Inorganic Chemistry

Article

pubs.acs.org/IC

Steric Effect on the Nucleophilic Reactivity of Nickel(III) Peroxo Complexes

Jalee Kim,[†,‡] Bongki Shin,[†,‡] Hyunjeong Kim,[†] Junhyung Lee,[†] Joongoo Kang,[†] Sachiko Yanagisawa,[§] Takashi Ogura,[§] Hideki Masuda,[⊥] Tomohiro Ozawa,[⊥] and Jaeheung Cho*[,†]

[†]Department of Emerging Materials Science, DGIST, Daegu 711-873, Korea

[§]Picobiology Institute, Graduate School of Life Science, University of Hyogo, Hyogo 678-1297, Japan

[⊥]Department of Frontier Materials, Graduate School of Engineering, Nagoya Institute of Technology, Nagoya 466-8555, Japan

Supporting Information

ABSTRACT: A set of nickel(III) peroxo complexes bearing tetraazamacrocyclic ligands, $[Ni^{III}(TBDAP)(O_2)]^+$ (TBDAP = *N*,*N*′-di-*tert*-butyl-2,11-diaza[3.3](2,6)pyridinophane) and $[Ni^{III}(CHDAP)(O_2)]^+$ (CHDAP = *N*,*N*′-dicyclohexyl-2,11-diaza[3.3](2,6)pyridinophane), were prepared by reacting $[Ni^{II}(TBDAP)(NO_3)(H_2O)]^+$ and $[Ni^{II}(CHDAP)(NO_3)]^+$, respectively, with H_2O_2 in the presence of triethylamine. The mononuclear nickel(III) peroxo complexes were fully characterized by various physicochemical methods, such as UV−vis, electrospray ionization mass spectrometry, resonance Raman, electron paramagnetic resonance, and X-ray analysis. The spectroscopic and structural characterization clearly shows that the NiO_2 cores are almost identical where the peroxo ligand is bound in a side-on fashion. However, the different steric properties of the supporting ligands were confirmed by X-ray crystallography, where the CHDAP ligand gives enough space around the Ni core compared to the TBDAP ligand. The nickel(III) peroxo complexes showed reactivity in the oxidation of aldehydes. In the aldehyde deformylation reaction, the nucleophilic reactivity of the nickel(III) peroxo complexes was highly dependent on the steric properties of the macrocyclic ligands, with a reactivity order of $[Ni^{III}(TBDAP)(O_2)]^+$ < $[Ni^{III}(CHDAP)(O_2)]^+$. This result provides fundamental insight into the mechanism of the structure (steric)−reactivity relationship of metal peroxo intermediates.

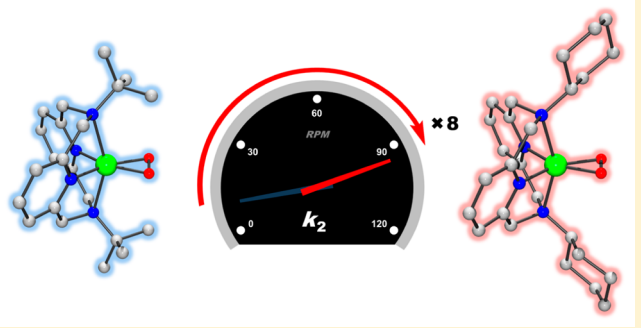

INTRODUCTION

Mononuclear metal−O_2 adducts, such as metal peroxo species, are the crucial reactive intermediates in enzymatic reactions as well as oxidative catalytic processes. For example, manganese(III) peroxo intermediates have been invoked as reactive species in manganese-containing enzymes including oxalate oxidase, catalase, and superoxide dismutase.[1−3] In addition, mononuclear iron(III) peroxo species are often observed in the activation of dioxygen by iron enzymes (e.g., cytochromes P450 and Rieske dioxygenases).[4−6] In synthetic model chemistry, iron(III) peroxo complexes have been prepared and characterized with various physicochemical methods, and the reactivities of the models were investigated in biomimetic reactions.[7] Some of us and others have also reported the synthesis and characterization of an iron(III) peroxo complex, $[Fe^{III}(TMC)(O_2)]^+$, which is capable of conducting aldehyde deformylation,[8] and highlighted its unique conversion procedures; upon protonation, the iron(III) peroxo complex is completely converted to an iron(III) hydroperoxo complex, which readily undergoes O−O bond cleavage, affording the formation of an iron(IV) oxo complex.[8a,9]

Recent advances in biomimetic chemistry have a chance to generate a series of mononuclear side-on metal(III) peroxo complexes bearing N-tetramethylated macrocyclic ligands, where the spectroscopic properties and reactivities of the metal(III) peroxo species are profoundly affected by the ring-size effect of the supporting ligands.[10] A notable example is the formation of a side-on nickel(III) peroxo complex with the 12-membered macrocycle and an end-on nickel(II) superoxo complex bearing the 14-membered macrocycle.[11] The former has a nucleophilic character (e.g., aldehyde deformylation), while the latter shows electrophilic reactivity (e.g., phosphine oxidation) toward organic substrates. The ring-size effect in these studies does result in significant changes in the structures formed and the reactivity patterns of the nickel−O_2 species.[11,12]

It is necessary to understand the role of controlling factors related to the nature of the supporting ligand, which influences the resulting reactivity patterns. To the best of our knowledge, the steric effect has never been observed in the reactivity of mononuclear metal(III) peroxo complexes toward external

Received: February 8, 2015
Published: June 12, 2015

DOI: 10.1021/acs.inorgchem.5b00294
Inorg. Chem. 2015, 54, 6176−6183

substrates, although the electronic effect on the reactivity of the nickel alkylperoxo complex has been reported very recently.[13] Here, we report a new set of nickel(III) peroxo complexes with TBDAP (*N*,*N*′-di-*tert*-butyl-2,11-diaza[3.3](2,6)pyridinophane) and CHDAP (*N*,*N*′-dicyclohexyl-2,11-diaza[3.3](2,6)-pyridinophane) ligands (Scheme 1), which give steric differences in NiO_2 cores. The nickel(III) peroxo complexes $[Ni^{III}(TBDAP)(O_2)]^+$ (**1**) and $[Ni^{III}(CHDAP)(O_2)]^+$ (**2**) were characterized by a wide range of physicochemical methods. The intermediates **1** and **2** have been employed in exploring the steric effect on the reactivity of the nickel(III) peroxo species toward organic substrates in a nucleophilic reaction.

Scheme 1. Macrocyclic Ligands Used in This Study

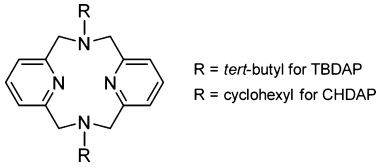

RESULTS AND DISCUSSION

CHDAP was prepared by a modification of the reported procedure [see the Supporting Information (SI), Experimental Section].[14] The CHDAP ligand was characterized by elemental analysis, electrospray ionization mass spectrometry (ESI-MS), and ^1H and ^{13}C NMR methods (see the SI, Experimental Section and Figures S1−S3).

The starting nickel complexes, $[Ni^{II}(TBDAP)(NO_3)(H_2O)]^+$ and $[Ni^{II}(CHDAP)(NO_3)]^+$, were prepared by reacting $Ni(NO_3)_2{\cdot}6H_2O$ with the corresponding TBDAP and CHDAP ligands, respectively. The UV−vis spectrum of $[Ni^{II}(TBDAP)(NO_3)(H_2O)]^+$ in CH_3CN exhibits three absorption bands at 645 nm (ε = 10 M^{-1} cm^{-1}), 823 nm (ε = 10 M^{-1} cm^{-1}), and 1066 nm (ε = 25 M^{-1} cm^{-1}) (Figure 2a). The ESI-MS spectrum of $[Ni^{II}(TBDAP)(NO_3)(H_2O)]^+$ shows three signals at mass-to-charge ratios of *m*/*z* 225.6, 246.1, and 472.2 for $[Ni(TBDAP)(CH_3CN)]^{2+}$ (calcd *m*/*z* 225.6), $[Ni(TBDAP)(CH_3CN)_2]^{2+}$ (calcd *m*/*z* 246.1), and $[Ni(TBDAP)(NO_3)]^+$ (calcd *m*/*z* 472.2), respectively (see the SI, Figure S4). The X-ray crystal structure of $[Ni(TBDAP)(NO_3)(H_2O)](NO_3)$ shows a six-coordinated nickel(II) ion with four nitrogen atoms from the TBDAP ligand and two oxygen atoms from a monodentate nitrate and water (Figure 1a and Table 1). Selected bond lengths and angles are listed in the SI, Table S1.

The UV−vis spectrum of $[Ni^{II}(CHDAP)(NO_3)]^+$ in CH_3CN shows three absorption bands at 588 nm (ε = 15 M^{-1} cm^{-1}), 835 nm (ε = 25 M^{-1} cm^{-1}), and 1010 nm (ε = 45 M^{-1} cm^{-1}) (Figure 5a). The ESI-MS spectrum of $[Ni^{II}(CHDAP)(NO_3)]^+$ exhibits two intense ion peaks at *m*/*z* 251.7 and 524.3, whose mass and isotope distribution patterns correspond to $[Ni(CHDAP)(CH_3CN)]^{2+}$ (calcd *m*/*z* 251.6) and $[Ni(CHDAP)(NO_3)]^+$ (calcd *m*/*z* 524.2), respectively (see the SI, Figure S5). The molecular structure of the cationic part for $[Ni(CHDAP)(NO_3)](NO_3)(CH_3OH)$ is shown in Figure 1b. The complex has a six-coordinated nickel(II) ion with the CHDAP ligand and a symmetrically coordinated bidentate nitrate anion. Selected bond lengths and angles are listed in the SI, Table S1.

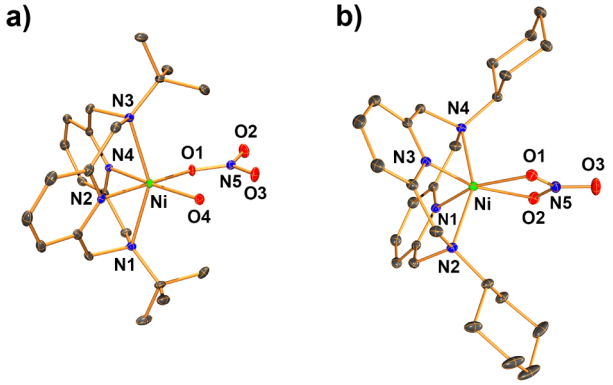

Figure 1. ORTEP plots of (a) $[Ni(TBDAP)(NO_3)(H_2O)]^+$ and (b) $[Ni(CHDAP)(NO_3)]^+$ with thermal ellipsoids drawn at the 30% probability level. Hydrogen atoms are omitted for clarity.

Synthetic procedures for nickel−O_2 complexes bearing TBDAP and CHDAP ligands are illustrated in Scheme 2. **1** was prepared by adding 5 equiv of H_2O_2 to a reaction solution containing $[Ni^{II}(TBDAP)(NO_3)(H_2O)]^+$ in the presence of 2 equiv of triethylamine (TEA) in CH_3CN at 25 °C; the color of the solution changed from blue to brown. Complex **1** persisted for several hours at 0 °C so that we were able to isolate and use it in spectroscopic and structural characterization. The UV−vis spectrum of **1** in CH_3CN at 25 °C shows two absorption bands at ∼560 nm (ε = 15 M^{-1} cm^{-1}) and 1040 nm (ε = 45 M^{-1} cm^{-1}) (Figure 2a). The ESI-MS spectrum of **1** exhibits a prominent signal at *m*/*z* 442.2 (Figure 2b), whose mass and isotope distribution patterns correspond to $[Ni(TBDAP)(O_2)]^+$ (calcd *m*/*z* 442.2). When the reaction was carried out with isotopically labeled $H_2{}^{18}O_2$, a mass peak corresponding to $[Ni(TBDAP)(^{18}O_2)]^+$ appeared at *m*/*z* 446.2 (calcd *m*/*z* 446.2) (Figure 2b, inset). The shift in four mass units upon substitution of ^{16}O with ^{18}O demonstrates that **1** contains two oxygen atoms.

The resonance Raman spectrum of **1** collected using 442 nm excitation in CD_3CN at −20 °C shows a resonance-enhanced vibration at 989 cm^{-1} (Figure 2c), which is tentatively assigned to ν(O−O) based on its frequency and a good correlation between the O−O bond length and O−O stretching frequency of **1** (vide infra).[15] This value is comparable to those reported for side-on nickel(III) peroxo complexes, such as $[Ni(12\text{-}TMC)(O_2)]^+$ (1002 cm^{-1}) and $[Ni(13\text{-}TMC)(O_2)]^+$ (1008 cm^{-1}),[10c,11a] indicating the peroxo character of the O_2 unit in **1**.

The X-band electron paramagnetic resonance (EPR) spectrum of **1** exhibits an axial signal with *g* values of 2.19 and 2.02 (Figure 2d), which is a typical $(d_{z^2})^1$ electron configuration observed for nickel(III) complexes.[16] Spin quantification finds that the EPR signal corresponds to 89% of the total nickel content in the sample (see the Experimental Section). The spin state of **1** in a CH_3CN solution was further determined using the ^1H NMR spectroscopy method of Evans,[17] and the room temperature magnetic moment of 2.3 μ_B clearly indicates an $S = {}^1/_2$ ground state.

The X-ray crystal structure of $[Ni(TBDAP)(O_2)](ClO_4)(0.5CH_2Cl_2)$ (**1**-$ClO_4{\cdot}0.5CH_2Cl_2$) revealed a mononuclear side-on nickel−O_2 complex in a distorted octahedral geometry arising from the triangular NiO_2 moiety with a small bite angle of 44.19(7)° (Figure 3). The O−O bond length (1.401(2) Å) of **1** is slightly longer than those of $[Ni(12\text{-}TMC)(O_2)]^+$ (1.386 Å) and $[Ni(13\text{-}TMC)(O_2)]^+$ (1.383 Å)[10c,11a] and lies well

DOI: 10.1021/acs.inorgchem.5b00294
Inorg. Chem. 2015, 54, 6176−6183

Table 1. Crystal Data and Structure Refinements for $[Ni(TBDAP)(NO_3)(H_2O)](NO_3)$, $[Ni(CHDAP)(NO_3)](NO_3)(CH_3OH)$, and 1-$ClO_4$·0.5$CH_2Cl_2$

	$[Ni(TBDAP)(NO_3)(H_2O)](NO_3)$	$[Ni(CHDAP)(NO_3)](NO_3)(CH_3OH)$	1-ClO_4·0.5CH_2Cl_2
empirical formula	$C_{22}H_{34}N_6NiO_7$	$C_{27}H_{40}N_6NiO_7$	$C_{22.5}H_{33}Cl_2N_4NiO_6$
fw	553.26	619.36	585.14
temperature (K)	100(2)	100(2)	100(2)
cryst syst/space group	orthorhombic, *Pbca*	triclinic, $P\bar{1}$	monoclinic, *C*2/*c*
unit cell dimens			
a (Å)	15.2958(5)	10.6798(2)	30.9602(6)
b (Å)	16.4819(6)	11.8168(2)	12.8498(2)
c (Å)	19.9118(8)	12.9559(2)	13.7307(2)
α (deg)	90	64.1040(10)	90.00
β (deg)	90	82.1330(10)	105.7590(10)
γ (deg)	90	78.9810(10)	90.00
volume (Å^3)	5019.8(3)	1441.11(4)	1047.70(5)
Z	8	2	8
calcd density (g cm^{-3})	1.464	1.427	1.479
abs coeff (mm^{-1})	0.827	0.729	0.986
reflns collected	104898	24970	46826
indep reflns [*R*(int)]	4018 [0.0804]	7001 [0.0187]	6538 [0.0360]
refinement method	full-matrix least squares on F^2	full-matrix least squares on F^2	full-matrix least squares on F^2
data/restraints/param	4018/0/339	7001/0/372	6538/0/327
GOF on F^2	1.001	1.037	1.040
final *R* indices [$I > 2\sigma(I)$]	R1 = 0.0324, wR2 = 0.1037	R1 = 0.0261, wR2 = 0.0702	R1 = 0.0341, wR2 = 0.0820
R indices (all data)	R1 = 0.0477, wR2 = 0.1239	R1 = 0.0274, wR2 = 0.0713	R1 = 0.0464, wR2 = 0.0874

Scheme 2. Synthetic Procedures for Mononuclear Nickel(III) Peroxo Complexes

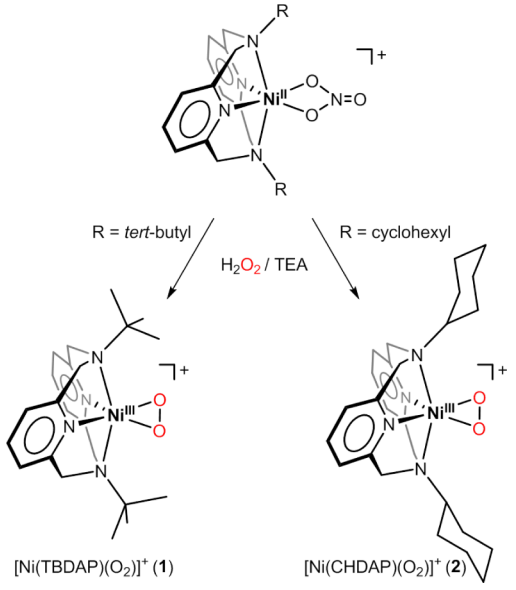

within the metal peroxo category (~1.4–1.5 Å).[17] The average Ni–N_{axial} bond distance (2.2677 Å) is considerably longer than the average Ni–$N_{equatorial}$ bond distance (1.9194 Å). This elongation of the axial bonds is attributable to the Jahn–Teller effect arising from a low-spin d^7 electron configuration (vide supra). The two *N*-*tert*-butyl groups of the TBDAP ligand are oriented syn to the peroxo ligand, affording steric hindrance to protect the NiO_2 moiety. In addition, a good correlation was observed when the O–O bond length and O–O stretching frequency of **1** was fitted in the plot of O–O stretching frequency versus O–O bond length for side-on metal–O_2 complexes (Figure 4).[18] On the basis of the structural and spectroscopic data, **1** is assigned as a side-on nickel(III) peroxo complex.

2 was obtained by a method similar to that of **1** with the corresponding CHDAP ligand (Scheme 2). The UV–vis spectrum of **2** in CH_3CN at 25 °C shows two absorption bands at 584 nm (ε = 35 M^{-1} cm^{-1}) and 950 nm (ε = 70 M^{-1} cm^{-1}) (Figure 5a), which are comparable to those of **1**. The ESI-MS spectrum of **2** shows a prominent signal at *m*/*z* 494.2 (Figure 5b), whose mass and isotope distribution patterns correspond to $[Ni(CHDAP)(O_2)]^+$ (calcd *m*/*z* 494.2). The isotope labeling experiment with $H_2{}^{18}O_2$ exhibited the expected signal at *m*/*z* 498.2 for $[Ni(CHDAP)(^{18}O_2)]^+$ (calcd *m*/*z* 498.2) (Figure 5b, inset). Upon 442 nm excitation at −20 °C, the resonance Raman spectrum of ^{16}O-labeled **2** in CD_3CN exhibits an isotopically sensitive band at 988 cm^{-1}, which shifts to 919 cm^{-1} upon ^{18}O substitution (Figure 5c). The O–O stretching vibration of **2** is very similar to that of **1**. The EPR spectrum of a frozen CH_3CN solution of **2** at 20 K shows an axial signal with *g* values of 2.17 and 2.03 (Figure 5d). Spin quantification finds that the EPR signal corresponds to 95% of the total nickel content in the sample. The room temperature magnetic moment of 2.2 μ_B,[17] determined using the ^{1}H NMR Evans method, is consistent with an $S = {}^1/_2$ ground state of **2**. The similarity of these spectroscopic features to those of **1** leads us to assign **2** as a side-on nickel(III) peroxo complex.

Density functional theory (DFT) calculations were performed to evaluate the geometric information on **2**. In order to gauge the reliability of the calculations, structural comparisons were made between the crystal structure of **1** and that calculated by DFT,[19] where the root-mean-square deviation (RMSD) was calculated to be 0.03 Å. Because some differences are expected when the gas-phase calculated structures are compared with crystal forms, the structural quality of the calculations gave credibility to the subsequent calculations. The NiO_2 geometry of **2** is, as expected, of the side-on type with the metal ligand atoms in an octahedral fashion, which is similar to

DOI: 10.1021/acs.inorgchem.5b00294
Inorg. Chem. 2015, 54, 6176–6183

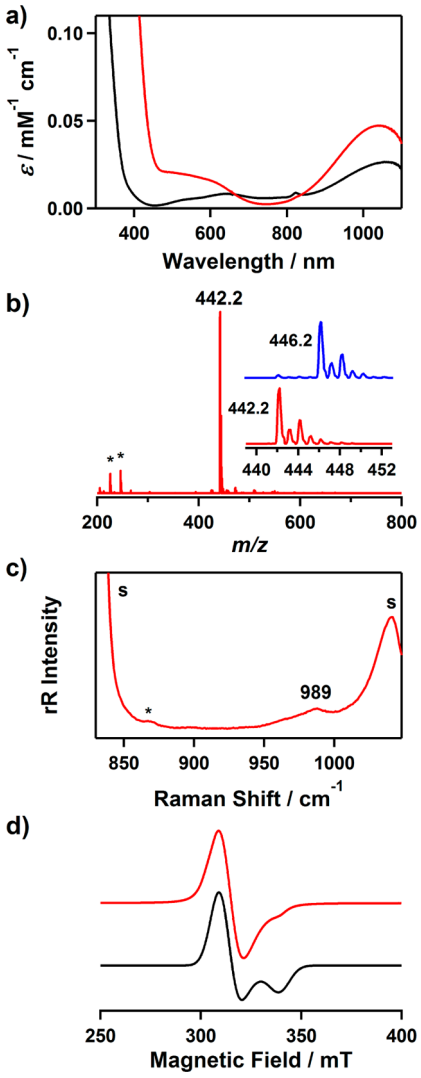

Figure 2. (a) UV−vis spectra of $[Ni^{II}(TBDAP)(NO_3)(H_2O)]^+$ (black line) and **1** (red line) in CH_3CN at 25 °C. (b) ESI-MS spectrum of **1** in CH_3CN at −20 °C. The minor peaks at m/z 225.7 and 246.2 labeled with asterisks are assignable to $[Ni(TBDAP)(CH_3CN)]^{2+}$ and $[Ni(TBDAP)(CH_3CN)_2]^{2+}$, respectively. The inset shows the observed isotope distribution patterns for $[Ni^{III}(TBDAP)(^{16}O_2)]^+$ (lower) and $[Ni^{III}(TBDAP)(^{18}O_2)]^+$ (upper). (c) Resonance Raman spectra of **1** (32 mM) obtained upon excitation at 442 nm in CD_3CN at −20 °C. An asterisk indicates the peak of H_2O_2. (d) X-band EPR spectrum (red) and simulation (black) of **1** in frozen CH_3CN at 20 K. Instrumental parameters: microwave power = 1 mW, frequency = 9.646 GHz, sweep width = 0.15 T, modulation frequency = 100 kHz, and modulation amplitude = 1 mT.

that of **1** (Figure 6). DFT calculations show that the steric bulk yields slightly longer metal−ligand bonds [avg. d(Ni−N_{axial}) = 2.30 Å for **1** and 2.23 Å for **2**; see the SI, Table S2]. However, the elongated Ni−N_{axial} bonds do not significantly affect the NiO_2 core structures [d(O−O) = 1.36 Å for **1** and 1.36 Å for **2**; avg. d(Ni−O) = 1.86 Å for **1** and 1.87 Å for **2**], consistent with nearly the same Raman frequencies of O_2 [ν(O−O) = 989 cm^{-1} for **1** and 988 cm^{-1} for **2**].

It has been noted that mononuclear metal peroxo species react with aldehydes to give the corresponding deformylated products.[5a,20] In order to investigate the steric effect on the reactivity of metal peroxo species, we carried out the reaction of 2-phenylpropionaldehyde (2-PPA) with **1** and **2**. Upon the

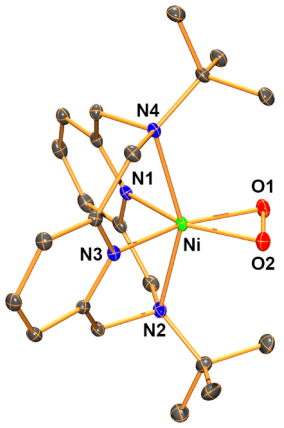

Figure 3. ORTEP plot of **1** with thermal ellipsoids drawn at the 30% probability level. Hydrogen atoms are omitted for clarity. Selected bond lengths (Å) and angles (deg): Ni−O1 1.8589(14), Ni−O2 1.8670(14), Ni−N1 1.9195(15), Ni−N2 2.2453(16), Ni−N3 1.9193(15), Ni−N4 2.2901(15), O1−O2 1.401(2); O1−Ni−O2 44.19(7), Ni−O1−O2 68.21(8), Ni−O2−O1 67.60(8).

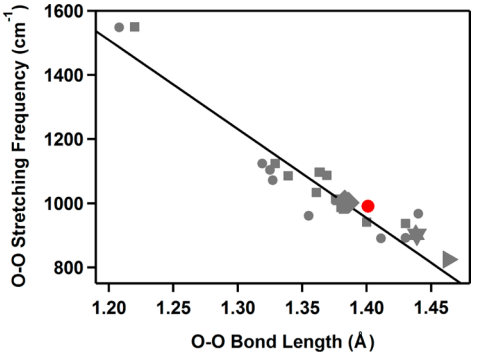

Figure 4. Plot of O−O stretching frequency (cm^{-1}) versus O−O bond distance (Å) for side-on metal−O_2 complexes. The gray points represent experimental and theoretical data previously reported.[10a,c] The solid line represents a least-squares linear fit of the experimental and theoretical data. **1** (red ●) is included in the diagram.

addition of 2-PPA to **1** in CH_3CN/CH_3OH (1:1) at 25 °C, the characteristic UV−vis absorption bands of **1** disappeared with pseudo-first-order decay (Figure 7a), and product analysis of the reaction solution revealed that acetophenone (71 ± 5%) was produced in the oxidation of 2-PPA. In addition, **1** is converted to its nickel(II) precursor complex after the reaction was completed, which was confirmed by ESI-MS (see the SI, Figure S6). The pseudo-first-order rate constants, monitored at 560 nm, increased proportionally with an increase of the concentration of 2-PPA, affording a second-order rate constant (k_2) of 7.4 × 10^{-3} M^{-1} s^{-1} (Figure 8). The activation parameters for aldehyde deformylation of **1** between 278 and 308 K were determined to be $\Delta H^{\ddagger}$ = 67 kJ mol^{-1} and $\Delta S^{\ddagger}$ = −62 J mol^{-1} K^{-1} (Figure 7b).

The reaction of **1** with para-substituted benzaldehydes, which have electron-donating and -withdrawing substituents at the para position of the phenyl group (*p*-X−Ph−CHO; X = Me, F, H, Cl, Br), provides mechanistic insight into the nature of the peroxo group in **1** (Table S3 in the SI). The Hammett plot of the pseudo-first-order rate constants versus σ_p^+ afforded a ρ value of 4.4(3) (Figure 7c), which is consistent with the nucleophilic character of **1** in the oxidation of aldehydes. Product analysis of the resulting solution revealed the

DOI: 10.1021/acs.inorgchem.5b00294
Inorg. Chem. 2015, 54, 6176−6183

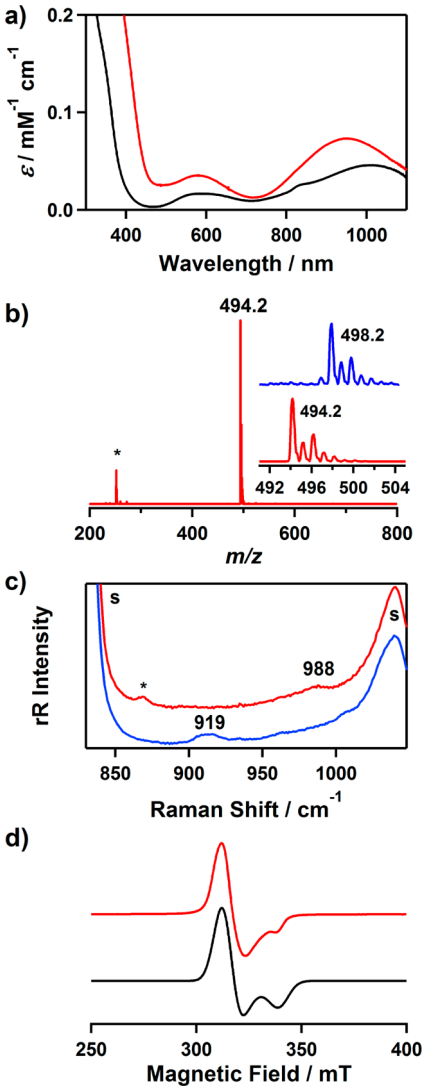

Figure 5. (a) UV−vis spectra of $[Ni^{II}(CHDAP)(NO_3)]^+$ (black line) and **2** (red line) in CH_3CN at 25 °C. (b) ESI-MS spectrum of **2** in CH_3CN at −20 °C. The minor peak at m/z 251.6 labeled with an asterisk is assignable to $[Ni(CHDAP)(CH_3CN)]^{2+}$. The inset shows the observed isotope distribution patterns for $[Ni(CHDAP)(^{16}O_2)]^+$ (lower) and $[Ni(CHDAP)(^{18}O_2)]^+$ (upper). (c) Resonance Raman spectra of **2** (32 mM) obtained upon excitation at 442 nm in CD_3CN at −20 °C: **2** prepared with $H_2{}^{16}O_2$ (red line) and $H_2{}^{18}O_2$ (blue line). An asterisk indicates the peak of H_2O_2. (d) X-band EPR spectrum (red) and simulation (black) of **2** in frozen CH_3CN at 20 K. Instrumental parameters: microwave power = 1 mW, frequency = 9.646 GHz, sweep width = 0.15 T, modulation frequency = 100 kHz, and modulation amplitude = 1 mT.

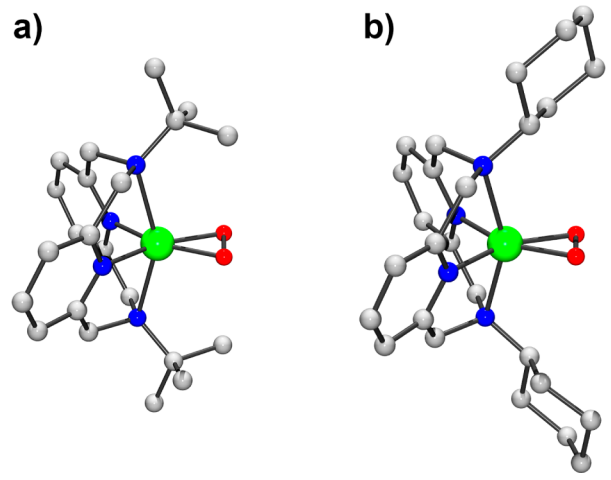

Figure 6. DFT-calculated structures for (a) **1** and (b) **2** (gray, C; blue, N; red, O; green, Ni). Hydrogen atoms are omitted for clarity.

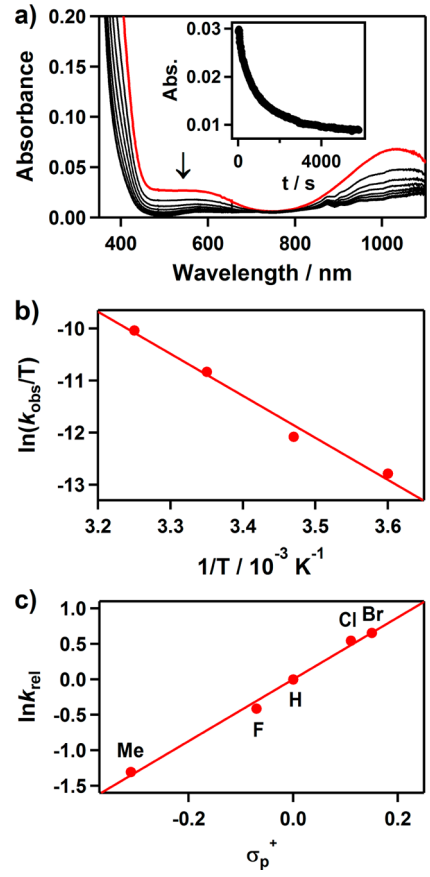

Figure 7. Reactions of **1** with aldehydes in CH_3CN/CH_3OH (1:1). (a) UV−vis spectral changes of **1** (2 mM) upon the addition of 100 equiv of 2-PPA at 25 °C. The inset shows the time course of the absorbance at 560 nm. (b) Plot of first-order rate constants against $1/T$ to determine activation parameters. (c) Hammett plot of ln k_{rel} against σ_p^+ of para-substituted benzaldehydes. The k_{rel} values were calculated by dividing k_{obs} of *p*-X−Ph−CHO (X = Me, F, H, Cl, Br) by k_{obs} of benzaldehyde at 25 °C.

formation of benzoic acid (94 ± 3%) as a product, as observed in the oxidation of benzaldehydes by metal peroxo complexes.[10a,20c] It is worth noting that **1** does not react with triphenylphosphine, thioanisole, and cyclohexadiene, which were used to test the electrophilic reactivity of model complexes.[10a] This observation, together with the result of the Hammett study, indicates that **1** has nucleophilic character.

Upon reaction of **2** with 2-PPA, the characteristic UV−vis absorption bands of **2** disappeared with a pseudo-first-order decay (see the SI, Figure S7a), and product analysis of the reaction solutions revealed the formation of acetophenone (90 ± 5%) in the oxidation of 2-PPA. After the reaction was completed, **2** is reduced to its nickel(II) precursor complex, which was confirmed by ESI-MS (see the SI, Figure S8). The pseudo-first-order rate constants increased proportionally with the substrate concentration (Figure 8), in which the second-

DOI: 10.1021/acs.inorgchem.5b00294
Inorg. Chem. 2015, 54, 6176−6183

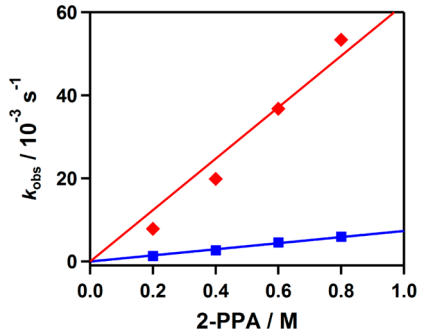

Figure 8. Kinetic studies of the reactions of **1** and **2** with 2-PPA in CH_3CN/CH_3OH (1:1) at 25 °C. Plots of k_{obs} against the 2-PPA concentration to determine second-order rate constants for the reactions of **1** (blue ■) and **2** (red ◆).

order rate constant (k_2 = 6.2 × 10^{-2} M^{-1} s^{-1} at 25 °C) was determined. The activation parameters were determined to be $\Delta H^{\ddagger}$ = 66 kJ mol^{-1} and $\Delta S^{\ddagger}$ = −48 J mol^{-1} K^{-1} (see the SI, Figure S7b). The effects of para substituents on the benzaldehyde oxidation process were investigated, and the Hammett plot afforded ρ = 4.3(7) (see the SI, Table S3 and Figure S7c). We have observed the formation of benzoic acid (84 ± 3%) as a product in the oxidation of benzaldehyde. The positive value is consistent with the process involving nucleophilic character.

The cyclic voltammograms of nickel(II) chloride complexes with TBDAP and CHDAP in CH_3CN exhibit a quasi-reversible redox couple at $E_{1/2}$ = 0.56 and 0.57 V (vs Fc^+/Fc), respectively, as shown in Figure 9 with data collected in

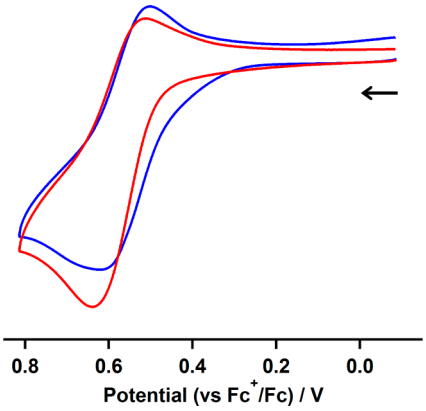

Figure 9. Cyclic voltammograms of $[Ni(TBDAP)Cl_2]$ (blue) and $[Ni(CHDAP)Cl_2]$ (red) in CH_3CN (1 mM) containing 0.1 M Bu_4NClO_4 at room temperature (working electrode, Pt; counter electrode, Pt; reference electrode, Ag/Ag^+; scan rate = 100 mV).

Table 2.[21] The redox couples correspond to the one-electron oxidation of the Ni^{II} state to the Ni^{III} state.[22] The data show that the redox couples are almost identical.

Table 2. Electrochemical Data for the Oxidation of Nickel(II) Complexes with TBDAP and CHDAP at Room Temperature at Scan Rate = 0.1 V

complex	$E_{1/2}$(II/III) (ΔE) vs Fc^+/Fc (V)
$[Ni^{II}(TBDAP)Cl_2]$	0.56 (0.12)
$[Ni^{II}(CHDAP)Cl_2]$	0.57 (0.13)

Upon a comparison of the kinetic data of **1** (k_2 = 7.4 × 10^{-3} M^{-1} s^{-1}) and **2** (k_2 = 6.2 × 10^{-2} M^{-1} s^{-1}) in the oxidation of 2-PPA (Figure 8), it can be seen that the reactivity of **2** is greater than that of **1** in the aldehyde deformylation reaction. The differential reactivity is attributable to the structural features of **1** and **2** (Scheme 2 and Figures 3 and 6). The *tert*-butyl groups of **1** provide the steric hindrance of the NiO_2 moiety. However, the cyclohexyl groups of **2** give sufficient space around the NiO_2 core to allow the substrate to approach the peroxo moiety (see the SI, Figure S9).[23] These results were also elucidated by the difference of the activation enthalpy values of 67 kJ mol^{-1} for **1** and 66 kJ mol^{-1} for **2**, and the difference of $\Delta\Delta G^{\ddagger}$ between **1** and **2** is 5 kJ mol^{-1}. In addition, almost identical O−O stretching frequencies of **1** (989 cm^{-1}) and **2** (988 cm^{-1}) suggest that the difference in the electronic effect of the *tert*-butyl and cyclohexyl groups on the NiO_2 cores is negligible. This result is consistent with the identical ρ values from the Hammett plots (vide supra). However, we cannot rule out a small electronic effect on the NiO_2 cores by changing the *tert*-butyl to cyclohexyl groups.[24] Consequently, through control of the steric factor from *tert*-butyl to cyclohexyl groups, the aldehyde deformylation reaction by the nickel(III) peroxo complexes is facilitated and the reaction rate is enhanced ∼8 times.

■ CONCLUSIONS

The structure and reactivity of metal−O_2 adducts in the oxidation of organic compounds are of crucial interest in enzymatic activity, organic synthesis, and industrial catalysis. A number of metal(III) peroxo complexes and their reactivity in aldehyde deformylation have been investigated. However, the steric effect on the reactivity of metal(III) peroxo species has not been reported yet. In this work, we synthesized mononuclear nickel(III) peroxo complexes bearing macrocyclic tetradentate N_4 ligands, $[Ni^{III}(TBDAP)(O_2)]^+$ (**1**) and $[Ni^{III}(CHDAP)(O_2)]^+$ (**2**). The intermediates were fully characterized with various physicochemical methods such as UV−vis, ESI-MS, resonance Raman, EPR, and X-ray analysis. Both **1** and **2** are capable of deformylating aldehydes, and the nucleophilic character of **1** and **2** was confirmed by positive Hammett ρ values of 4.4(3) and 4.3(7), respectively, which were obtained in the reaction of **1** and **2** with para-substituted benzaldehydes. A comparison of the reactivity of **1** and **2** in aldehyde deformylation reveals that the reactivity of **2** is ∼8 times greater than that of **1**. The results regarding the disparate steric effects of the *tert*-butyl groups for **1** and cyclohexyl groups for **2** are verified by spectroscopic and kinetic studies combined with structural analyses. DFT calculations support the experimental observations that the nucelophilic reactivity of the nickel(III) peroxo complexes is highly dependent on the steric properties of the supporting ligands.

■ EXPERIMENTAL SECTION

Materials. All chemicals obtained from Aldrich Chemical Co. were of the best available purity and were used without further purification unless otherwise indicated. Solvents were dried according to published procedures and distilled under argon prior to use.[25] $H_2{}^{18}O_2$ (95% ^{18}O-enriched and 0.89% $H_2{}^{18}O_2$ in water) was purchased from ICON Services Inc. (Summit, NJ). *N,N′*-Di-*tert*-butyl-2,11-diaza[3.3](2,6)-pyridinophane (TBDAP) was prepared by reacting 2,6-bis-(chloromethyl)pyridine with 2,6-bis[(*N*-*tert*-butylamino)methyl]-pyridine at 80 °C.[14] The synthetic procedures of the *N,N′*-dicyclohexyl-2,11-diaza[3.3](2,6)pyridinophane (CHDAP) ligand are given in the SI, Experimental Section. $[Ni(TBDAP)Cl_2]$ was prepared

DOI: 10.1021/acs.inorgchem.5b00294
Inorg. Chem. 2015, 54, 6176−6183

according to the literature method.[22] [Ni(CHDAP)Cl_2] was prepared by a modification of the reported procedure (see the SI, Experimental Section).[22]

Physical Methods. UV−vis spectra were recorded on a Hewlett-Packard 8453 diode-array spectrophotometer equipped with a UNISOKU Scientific Instruments for low-temperature experiments or with a circulating water bath. ESI-MS spectra were collected on a Waters (Milford, MA) Acquity SQD quadrupole mass instrument, by infusing samples directly into the source using a manual method. The spray voltage was set at 2.5 kV and the capillary temperature at 80 °C. Cold-spray-ionization time-of-flight mass spectrometry spectra were collected on a JEOL JMS-T100CS spectrometer. Resonance Raman spectra were obtained using a liquid-nitrogen-cooled charge-coupled detector (CCD-1024 × 256-OPEN-1LS, Horiba Jobin Yvon) attached to a 1-m single polychromator (MC-100DG, Ritsu Oyo Kogaku) with a 1200 grooves mm^{-1} holographic grating. An excitation wavelength of 441.6 nm was provided by a helium−cadmium laser (Kimmon Koha, IK5651R-G and KR1801C), with 20 mW power at the sample point. All measurements were carried out with a spinning cell (1000 rpm) at −20 °C. Raman shifts were calibrated with indene, and the accuracy of the peak positions of the Raman bands was ±1 cm^{-1}. The effective magnetic moments were determined using the modified ^{1}H NMR method of Evans at room temperature.[17,26,27] A WILMAD coaxial insert (sealed capillary) tube containing the blank acetonitrile-d_3 solvent [with 1.0% tetramethylsilane (TMS)] only was inserted into the normal NMR tubes containing the complexes dissolved in acetonitrile-d_3 (with 0.03% TMS). The chemical shift of the TMS peak (and/or solvent peak) in the presence of the paramagnetic metal complexes was compared to that of the TMS peak (and/or solvent peak) in the inner coaxial insert tube. The effective magnetic moment was calculated using the equation $\mu = 0.0618(\Delta\nu T/2fM)^{1/2}$, where f is the oscillator frequency (MHz) of the superconducting spectrometer, T is the absolute temperature, M is the molar concentration of the metal ion, and $\Delta\nu$ is the difference in frequency (Hz) between the two reference signals. Continuous-wave EPR spectra were taken at 20 K using an X-band Bruker EMX-plus spectrometer equipped with a dual-mode cavity (ER 4116DM). Low temperatures were achieved and controlled using an Oxford Instruments ESR900 liquid-helium quartz cryostat with an Oxford Instruments ITC503 temperature and gas flow controller. Variable amounts of $CuCl_2$ (0.5−1 mM) were used as a EPR standard for spin quantification. Product analysis was performed with high-performance liquid chromatography (HPLC; Waters Pump series P580) equipped with a variable-wavelength UV-200 detector and a Thermo Finnigan (Austin, TX) FOCUS DSQ (dual-stage quadrupole) mass spectrometer interfaced with a Finnigan FOCUS gas chromatograph. Quantitative analysis was made on the basis of a comparison of the HPLC peak integration between the products and authentic samples. ^{1}H and ^{13}C NMR spectra were measured with a Bruker AVANCE III-400 spectrometer.

Generation and Characterization of [Ni(TBDAP)(O_2)]$^+$ (1). The treatment of [Ni(TBDAP)$(NO_3)(H_2O)$](NO_3) (4 mM) with 5 equiv of H_2O_2 in the presence of 2 equiv of TEA in CH_3CN (2 mL) afforded the formation of a brown solution at 25 °C. Spectroscopic data, including UV−vis, ESI-MS, resonance Raman, and EPR, are reported in Figure 2. [Ni(TBDAP)$(^{18}O_2)$]$^+$ was prepared by adding 5 equiv of $H_2{}^{18}O_2$ (72 μL, 90% ^{18}O-enriched, 0.89% $H_2{}^{18}O_2$ in water) to a solution containing [Ni(TBDAP)$(NO_3)(H_2O)$](NO_3) (4 mM) and 2 equiv of TEA in CH_3CN (2 mL) at ambient temperature. Crystalline yield: 0.015 g (44%). UV−vis [CH_3CN; λ_{max}, nm (ε, M^{-1} cm^{-1})]: ∼560 (15), 1040 (45). ESI-MS (CH_3CN): m/z 442.2 for [Ni(TBDAP)(O_2)]$^+$. μ_{eff} = 2.3 μ_B. X-ray crystallographically suitable crystals were obtained by the slow diffusion of Et_2O into a CH_2Cl_2 solution of **1** in the presence of $NaClO_4$. ***Caution!*** *Perchlorate salts are potentially explosive and should be handled with care!*

Generation and Characterization of [Ni(CHDAP)(O_2)]$^+$ (2). The treatment of [Ni(CHDAP)(NO_3)]$(NO_3)(CH_3OH)$ (4 mM) with 5 equiv of H_2O_2 in the presence of 2 equiv of TEA in CH_3CN (2 mL) at 25 °C afforded a green solution. Spectroscopic data, including UV−vis, ESI-MS, resonance Raman, and EPR, are reported in Figure 5. [Ni(CHDAP)$(^{18}O_2)$]$^+$ was prepared by adding 5 equiv of $H_2{}^{18}O_2$ (72 μL, 90% ^{18}O-enriched, 0.89% $H_2{}^{18}O_2$ in water) to a solution containing [Ni(CHDAP)(NO_3)]$(NO_3)(CH_3OH)$ (4 mM) and 2 equiv of TEA in CH_3CN (2 mL) at ambient temperature. UV−vis [CH_3CN; λ_{max}, nm (ε, M^{-1} cm^{-1})]: 584 (35), 950 (70). ESI-MS (CH_3CN): m/z 494.2 for [Ni(CHDAP)(O_2)]$^+$. μ_{eff} = 2.2 μ_B.

X-ray Crystallography. Single crystals of [Ni(TBDAP)$(NO_3)(H_2O)$](NO_3), [Ni(CHDAP)(NO_3)]$(NO_3)(CH_3OH)$, and [Ni(TBDAP)(O_2)]$(ClO_4)(0.5CH_2Cl_2)$ (**1**-ClO_4·$0.5CH_2Cl_2$) were picked from solutions by a nylon loop (Hampton Research Co.) on a handmade copper plate mounted inside a liquid-nitrogen Dewar vessel at ca. −40 °C and mounted on a goniometer head in a dinitrogen cryostream. Data collections were carried out on a Bruker SMART APEX II CCD diffractometer equipped with a monochromator in the Mo Kα (λ = 0.71073 Å) incident beam. The CCD data were integrated and scaled using the Bruker *SAINT* software package, and the structure was solved and refined using *SHELXTL*, version 6.12.[28] Hydrogen atoms were located in the calculated positions except for those of water in [Ni(TBDAP)$(NO_3)(H_2O)$](NO_3). Hydrogen atoms on the water were found from the Fourier difference map. All non-hydrogen atoms were refined with anisotropic thermal parameters. Crystal data for [Ni(TBDAP)$(NO_3)(H_2O)$](NO_3): $C_{22}H_{34}N_6NiO_7$, orthorhombic, *Pbca*, Z = 8, a = 15.2958(5) Å, b = 16.4819(6) Å, c = 19.9118(8) Å, V = 5019.8(3) Å^3, μ = 0.827 mm^{-1}, ρ_{calcd} = 1.464 g cm^{-3}, R1 = 0.0324, wR2 = 0.1037 for 4018 unique reflections, 339 variables. Crystal data for [Ni(CHDAP)(NO_3)]$(NO_3)(CH_3OH)$: $C_{27}H_{40}N_6NiO_7$, triclinic, $P\bar{1}$, Z = 2, a = 10.6798(2) Å, b = 11.8168(2) Å, c = 12.9559(2) Å, α = 64.1040(10)°, β = 82.1330(10)°, γ = 78.9810(10)°, V = 1441.11(4) Å^3, μ = 0.729 mm^{-1}, ρ_{calcd} = 1.427 g cm^{-3}, R1 = 0.0261, wR2 = 0.0702 for 7001 unique reflections, 372 variables. Crystal data for **1**-ClO_4·$0.5CH_2Cl_2$: $C_{22.5}H_{33}Cl2N_4NiO_6$, monoclinic, *C*2/*c*, Z = 8, a = 30.9602(6) Å, b = 12.8498(2) Å, c = 13.7307(2) Å, β = 105.7590(10)°, V = 5257.20(15) Å^3, μ = 0.986 mm^{-1}, ρ_{calcd} = 1.479 g cm^{-3}, R1 = 0.0341, wR2 = 0.0820 for 6538 unique reflections, 327 variables. The crystallographic data for [Ni(TBDAP)$(NO_3)(H_2O)$](NO_3), [Ni(CHDAP)(NO_3)]$(NO_3)(CH_3OH)$, and **1**-ClO_4·$0.5CH_2Cl_2$ are listed in Table 1, and Table S1 in the SI lists the selected bond distances and angles. CCDC 1060970 for [Ni(TBDAP)$(NO_3)(H_2O)$](NO_3), 1026817 for [Ni(CHDAP)(NO_3)]$(NO_3)(CH_3OH)$, and 1026816 for **1**-ClO_4·$0.5CH_2Cl_2$ contain the supplementary crystallographic data for this paper. These data can be obtained free of charge via www.ccdc.cam.ac.uk/data_request/cif [or from the Cambridge Crystallographic Data Centre, 12 Union Road, Cambridge CB2 1EZ, U.K.; fax (+44) 1223-336-033 or e-mail deposit@ccdc.cam.ac.uk].

Computational Details. The structures of [Ni^{III}(TBDAP)(O_2)]$^+$ (**1**) and [Ni^{III}(CHDAP)(O_2)]$^+$ (**2**) in the gas phase were optimized using a nonlocal hybrid exchange-correlation functional (HSE06).[29] Spin-polarized DFT calculations were performed using the projector-augmented-wave method[30] and a plane-wave cutoff of 400 eV, as implemented in the VASP code.[30−32] Atomic structures were relaxed within 0.05 eV Å^{-1}. The RMSD for the X-ray diffraction and DFT structures of [Ni(TBDAP)(O_2)]$^+$ was calculated to be 0.03 Å. Hydrogen atoms were not considered for structural comparison because their atomic positions in the crystal structure cannot be accurately determined by X-ray diffraction.

Reactivity Studies. All reactions were run in an 1 cm UV cuvette by monitoring UV−vis spectral changes of the reaction solutions, and rate constants were determined by fitting the changes in absorbance at 560 nm for **1** and 934 nm for **2**. Reactions were run at least in triplicate, and the data reported represent the average of these reactions. In situ generated **1** and **2** were used in kinetic studies, such as the oxidation of 2-PPA in CH_3CN/CH_3OH (1:1) at 25 °C. After completion of the reactions, a pseudo-first-order fitting of the kinetic data allowed us to determine the k_{obs} values. Products formed in the oxidation of 2-PPA by **1** and **2** in CH_3CN/CH_3OH (1:1) at 25 °C were analyzed by HPLC. Products were analyzed by injecting the reaction mixture directly into the high-performance liquid chromatograph. Products were identified by comparison with authentic samples, and product yields were determined by comparison against standard areas prepared with authentic samples as an internal standard.

DOI: 10.1021/acs.inorgchem.5b00294
Inorg. Chem. 2015, 54, 6176−6183

■ ASSOCIATED CONTENT

Supporting Information

X-ray crystallographic data in CIF format, experimental details, Figures S1−S10, and Tables S1−S3. The Supporting Information is available free of charge on the ACS Publications website at DOI: 10.1021/acs.inorgchem.5b00294.

■ AUTHOR INFORMATION

Corresponding Author

*E-mail: jaeheung@dgist.ac.kr.

Author Contributions

‡These authors contributed equally.

Notes

The authors declare no competing financial interest.

■ ACKNOWLEDGMENTS

The research was supported by the NRF (Grants 2013K2A2A4000610 and 2014R1A1A2056051), the Ministry of Science, ICT and Future Planning (DGIST R&D Program 15-BD-0403 & 15-HRLA-02 and KCRC 2014M1A8A1049320), and the Ministry of Oceans and Fisheries (Marine Biotechnology Program 20150220) of Korea (to J.C.). H.M. and T.O. acknowledge financial support by the JSPS program for Accelerating Brain Circulation (R 2213). We are grateful to Drs. Young Jun Park and Yong-Min Lee (Ewha Womans University) for valuable discussions.

■ REFERENCES

(1) (a) Opaleye, O.; Rose, R.-S.; Whittaker, M. M.; Woo, E.-J.; Whittaker, J. W.; Pickersgill, R. W. *J. Biol. Chem.* **2006**, *281*, 6428−6433. (b) Borowski, T.; Bassan, A.; Richards, N. G. J.; Siegbahn, P. E. M. *J. Chem. Theory Comput.* **2005**, *1*, 686−693.

(2) Wu, A. J.; Penner-Hahn, J. E.; Pecoraro, V. L. *Chem. Rev.* **2004**, *104*, 903−938.

(3) (a) Grove, L. E.; Brunold, T. C. *Comments Inorg. Chem.* **2008**, *29*, 134−168. (b) Miller, A.-F. *Curr. Opin. Chem. Biol.* **2004**, *8*, 162−168. (c) Jackson, T. A.; Karapetian, A.; Miller, A.-F.; Brunold, T. C. *Biochemistry* **2005**, *44*, 1504−1520. (d) Bull, C.; Niederhoffer, E. C.; Yoshida, T.; Fee, J. A. *J. Am. Chem. Soc.* **1991**, *113*, 4069−4076. (e) Hearn, A. S.; Stroupe, M. E.; Cabelli, D. E.; Lepock, J. R.; Tainer, J. A.; Nick, H. S.; Silverman, D. N. *Biochemistry* **2001**, *40*, 12051−12058. (f) Hearn, A. S.; Tu, C.; Nick, H. S.; Silverman, D. N. *J. Biol. Chem.* **1999**, *274*, 24457−24460.

(4) Meunier, B., Ed. *Biomimetic Oxidations Catalyzed by Transition Metal Complexes*; Imperial College Press: London, 1999.

(5) (a) Wertz, D. L.; Valentine, J. S. *Struct. Bonding (Berlin)* **2000**, *97*, 37−60. (b) Vaz, A. D. N.; Roberts, E. S.; Coon, M. J. *J. Am. Chem. Soc.* **1991**, *113*, 5886−5887. (c) Akhtar, M.; Corina, D.; Miller, S.; Shyadehi, A. Z.; Wright, J. N. *Biochemistry* **1994**, *33*, 4410−4418.

(6) (a) Kovaleva, E. G.; Neibergall, M. B.; Chakrabarty, S.; Lipscomb, J. D. *Acc. Chem. Res.* **2007**, *40*, 475−483. (b) Wolfe, M. D.; Lipscomb, J. D. *J. Biol. Chem.* **2003**, *278*, 829−835. (c) Bassan, A.; Blomberg, M. R. A.; Siegbahn, P. E. M. *J. Biol. Inorg. Chem.* **2004**, *9*, 439−452. (d) Tarasev, M.; Ballou, D. P. *Biochemistry* **2005**, *44*, 6197−6207.

(7) (a) Costas, M.; Mehn, M. P.; Jensen, M. P.; Que, L., Jr. *Chem. Rev.* **2004**, *104*, 939−986. (b) Girerd, J.-J.; Banse, F.; Simaan, A. J. *Struct. Bonding (Berlin)* **2000**, *97*, 145−177.

(8) (a) Cho, J.; Jeon, S.; Wilson, S. A.; Liu, L. V.; Kang, E. A.; Braymer, J. J.; Lim, M. H.; Hedman, B.; Hodgson, K. O.; Valentine, J. S.; Solomon, E. I.; Nam, W. *Nature* **2011**, *478*, 502−505. (b) Annaraj, J.; Suh, Y.; Seo, M. S.; Kim, S. O.; Nam, W. *Chem. Commun.* **2005**, 4529−4531.

(9) Li, F.; Meier, K. K.; Cranswick, M. A.; Chakrabarti, M.; Heuvelen, K. M. V.; Münck, E.; Que, L., Jr. *J. Am. Chem. Soc.* **2011**, *133*, 7256−7259.

(10) (a) Cho, J.; Sarangi, R.; Nam, W. *Acc. Chem. Res.* **2012**, *45*, 1321−1330. (b) Cho, J.; Sarangi, R.; Kang, H. Y.; Lee, J. Y.; Kubo, M.; Ogura, T.; Solomon, E. I.; Nam, W. *J. Am. Chem. Soc.* **2010**, *132*, 16977−16986. (c) Cho, J.; Kang, H. Y.; Liu, L. V.; Sarangi, R.; Solomon, E. I.; Nam, W. *Chem. Sci.* **2013**, *4*, 1502−1508. (d) Yokoyama, A.; Han, J. E.; Cho, J.; Kubo, M.; Ogura, T.; Siegler, M. A.; Karlin, K. D.; Nam, W. *J. Am. Chem. Soc.* **2012**, *134*, 15269−15272. (e) Kang, H.; Cho, J.; Cho, K.-B.; Nomura, T.; Ogura, T.; Nam, W. *Chem.—Eur. J.* **2013**, *19*, 14119−14125. (f) Kim, D.; Cho, J.; Lee, Y.-M.; Sarangi, R.; Nam, W. *Chem.—Eur. J.* **2013**, *19*, 14112−14118. (g) Sarangi, R.; Cho, J.; Nam, W.; Solomon, E. I. *Inorg. Chem.* **2011**, *50*, 614−620.

(11) (a) Cho, J.; Sarangi, R.; Annaraj, J.; Kim, S. Y.; Kubo, M.; Ogura, T.; Solomon, E. I.; Nam, W. *Nat. Chem.* **2009**, *1*, 568−572. (b) Kieber-Emmons, M. T.; Annaraj, J.; Seo, M. S.; Heuvelen, K. M. V.; Tosha, T.; Kitagawa, T.; Brunold, T. C.; Nam, W.; Riordan, C. G. *J. Am. Chem. Soc.* **2006**, *128*, 14230−14231.

(12) Lam, B. M. T.; Halfen, J. A.; Young, V. G., Jr.; Hagadorn, J. R.; Holland, P. L.; Lledós, A.; Cucurull-Sánchez, L.; Novoa, J. J.; Alvarez, S.; Tolman, W. B. *Inorg. Chem.* **2000**, *39*, 4059−4072.

(13) Hikichi, S.; Kobayashi, C.; Yoshizawa, M.; Akita, M. *Chem.—Asian J.* **2010**, *5*, 2086−2092.

(14) Che, C.-M.; Li, Z.-Y.; Wong, K.-Y.; Poon, C.-K.; Mak, T. C. W.; Peng, S.-M. *Polyhedron* **1994**, *13*, 771−776.

(15) Unfortunately, we could not observe the ^{18}O-shifted band of **1** despite our great efforts. Because it was difficult to fully generate the ^{18}O-labeled **1** with 0.89% of $H_2{}^{18}O_2$. However, we confirmed that the ν(O−O) band disappeared when the solution was allowed to warm.

(16) Haines, R. I.; McAuley, A. *Coord. Chem. Rev.* **1981**, *39*, 77−119.

(17) Evans, D. F.; Jakubovic, D. A. *J. Chem. Soc., Dalton Trans.* **1988**, 2927−2933.

(18) (a) Cramer, C. J.; Tolman, W. B.; Theopold, K. H.; Rheingold, A. L. *Proc. Natl. Acad. Sci. U. S. A.* **2003**, *100*, 3635−3640. (b) Cramer, C. J.; Tolman, W. B. *Acc. Chem. Res.* **2007**, *40*, 601−608.

(19) Kohn, W.; Sham, L. J. *Phys. Rev.* **1965**, *140*, A1133−A1138.

(20) (a) Graham-Lorence, S.; Amarneh, B.; White, R. E.; Peterson, J. A.; Simpson, E. R. *Protein Sci.* **1995**, *4*, 1065−1080. (b) Seo, M. S.; Kim, J. Y.; Annaraj, J.; Kim, Y.; Lee, Y.-M.; Kim, S.-J.; Kim, J.; Nam, W. *Angew. Chem., Int. Ed.* **2007**, *46*, 377−380. (c) Jo, Y.; Annaraj, J.; Seo, M. S.; Lee, Y.-M.; Kim, S. Y.; Cho, J.; Nam, W. *J. Inorg. Biochem.* **2008**, *102*, 2155−2159.

(21) Unfortunately, we could not observe redox couples with the nickel(II) precursors. However, we can observe a quasi-reversible wave when we change counteranions of the nickel(II) precursors from nitrate to chloride.

(22) Khusnutdinova, J. R.; Rath, N. P.; Mirica, L. M. *Inorg. Chem.* **2013**, *52*, 3920−3932.

(23) Although we have not been able to determine the structure of **2**, the orientation and degree of steric property of *tert*-butyl versus cyclohexyl groups around the nickel(III) center may be deduced by the structural overlay of the nickel(II) precursor complexes.

(24) Barefield, E. K. *Coord. Chem. Rev.* **2010**, *254*, 1607−1627.

(25) Armarego, W. L. F., Perrin, D. D., Eds. *Purification of Laboratory Chemicals*; Pergamon Press: Oxford, U.K., 1997.

(26) Evans, D. F. *J. Chem. Soc.* **1959**, 2003−2005.

(27) Lölinger, J.; Scheffold, R. *J. Chem. Educ.* **1972**, 646−647.

(28) Sheldrick, G. M. *SHELXTL/PC for Windows XP*, version 6.12; Bruker AXS Inc.: Madison, WI, 2001.

(29) Krukau, A. V.; Vydrov, O. A.; Izmaylov, A. F.; Scuseria, G. E. *J. Chem. Phys.* **2006**, *125*, 224106.

(30) Blöchl, P. E. *Phys. Rev. B* **1994**, *50*, 17953.

(31) Kresse, G.; Furthmüller, J. *Phys. Rev. B* **1996**, *54*, 11169.

(32) Kresse, G.; Joubert, D. *Phys. Rev. B* **1999**, *59*, 1758.

DOI: 10.1021/acs.inorgchem.5b00294
Inorg. Chem. 2015, 54, 6176−6183